An Exact Solution for Ideal Dam-Break Floods on Steep Slopes

C. Ancey, M. Rentschler,

School of Architecture, Civil and Environmental Engineering, École Polytechnique Fédérale de Lausanne, 1015 Lausanne, Switzerland

R.M. Iverson, R.P. Denlinger

U.S. Geological Survey, Cascades Volcano Observatory, Vancouver, Washington, USA

C. Ancey, School of Architecture, Civil and Environmental Engineering, École Polytechnique Fédérale de Lausanne, 1015 Lausanne, Switzerland (christophe.ancey@epfl.ch)

Abstract. The shallow-water equations are used to model the flow resulting from the sudden release of a finite volume of frictionless, incompressible fluid down a uniform slope of arbitrary inclination. The hodograph transformation and Riemann's method make it possible to transform the governing equations into a linear system and then deduce an exact analytical solution expressed in terms of readily evaluated integrals. Although the solution treats an idealized case never strictly realized in nature, it is uniquely well-suited for testing the robustness and accuracy of numerical models used to model shallow-water flows on steep slopes.

1. Introduction

Dam-break floods on steep slopes occur in diverse settings. They may result from failure of either natural or manmade dams, and they have been responsible for the loss of thousands of lives [*Costa*, 1988]. Recent disasters resulting from dam-break floods on steep slopes include those at Fonte Santa mines, Portugal, in November 2006 and Taum Sauk, Missouri, USA, in December 2005.

Numerical solutions of the shallow-water equations are generally used to predict the behavior of dam-break floods, but exact analytical solutions suitable for testing these numerical solutions have been available only for floods with infinite volumes, horizontal beds, or both [e.g., *Zoppou and Roberts*, 2003]. Computational models used to simulate dam-break floods commonly produce numerical instabilities and/or significant errors close to the moving front when steep slopes and/or irregular terrain are present in the flood path. In part these problems reflect the complex interaction of phenomena not included in model formulation (e.g., intense sediment transport under time-dependent flow conditions), but in part they also reflect shortcomings in the numerical solution algorithms themselves. Therefore, it is important to obtain exact analytical solutions of the shallow-water equations that can be used to test the robustness of numerical models when they are applied to floods of finite volume on steep slopes. This paper presents a new solution for this purpose.

For the dam-break problem on a horizontal bed, many exact and approximate analytical solutions already exist. For example, *Ritter* [1892] addressed the case of an infinite volume of fluid suddenly released on a frictionless plane. An exact solution for a dam-break flood of finite volume on a frictionless bed was not presented until *Hogg* [2006] analyzed the finite-volume lock-exchange problem. The more realistic case involving a rough bed (represented by a Chézy-like friction force) has been addressed by a number of authors, including *Whitham* [1954], *Dressler* [1952], and *Hogg and Pritchard* [2004], but only asymptotic solutions have been developed to date. Taking into account a nonuniform velocity distribution in the vertical direction leads to mathematical difficulties, but exact self-similar solutions can still be obtained for floods with variable inflow (i.e., the released volume is a function of time) [*Ancey et al.*, 2006, 2007].

For sloping beds, most dam-break solutions developed to date employ approximations of the shallow-water equations, in which inertia or pressure-gradient terms have been neglected. Such assumptions typically lead to a kinematic wave approximation, which enables substantial simplification because the mass and momentum balances making up the shallow-water equations are transformed into a single nonlinear diffusion equation [*Hunt*, 1983; *Daly and Porporato*, 2004a, b; *Chanson*, 2006]. Exact solutions of the shallow-water equations for steep slopes have been obtained for infinite-volume dam-break floods [*Shen and Meyer*, 1963; *Mangeney et al.*, 2000; *Karelsky et al.*, 2000; *Peregrine and Williams*, 2001], and the case of a finite-volume flood has been investigated by *Dressler* [1958] and later by *Fernandez-Feria* [2006], who provided a partial solution by computing the position and velocity of the surge front and rear. *Savage and Hutter* [1989] constructed two similarity solutions known as the parabolic cap and M-wave, but these differ from the long-time asymptotic solution of the problem investigated here.

In this paper we present a new analytical solution of the shallow-water equations for a situation in which a finite volume of an ideal (frictionless) fluid is instantaneously released from behind a dam on a steep slope. Although frictionless flows never occur in real fluids, the frictionless case constitutes an unambiguous end member as well as a clear target case for testing numerical models [*Zoppou and Roberts*, 2003]. Our solution strategy is mostly identical to that used by *Hogg* [2006] for the lock-exchange problem, with some additional complications that we shall detail later. We begin our analysis by using the characteristics of the shallow-water equations to infer the positions of the flow front and tail at all times. We then employ the hodograph transformation, which converts the nonlinear shallow-water equations into a linear system by exchanging the roles of the dependent and independent variables. An integral form of the exact solution of the linear equations is then obtained using Riemann's method. This method, seldom used in open-channel hydraulics, is well established in some other fields where hyperbolic equations similar to the shallow-water equations arise. Typical examples include gas dynamics [*Courant and Friedrich*, 1948], collapse of a granular column [*Kerswell*, 2005], and tsunami or swash run-up on a shore [*Carrier and Greenspan*, 1958].

2. Governing equations

2.1. Flow-depth averaged equations

The nonlinear, one-dimensional shallow-water (Saint-Venant) equations provide a suitable approximation for modeling water surges over a wide, uniformly sloping bed inclined at an angle θ with respect to the horizontal (Figure 1). If the effects of friction are neglected (see Appendix A), these equations may be written as

$$\frac{\partial}{\partial \hat{t}}\hat{h} + \frac{\partial}{\partial \hat{x}}(\hat{h}\hat{u}) = 0, \quad (1)$$

$$\frac{\partial}{\partial \hat{t}}\hat{u} + \hat{u}\frac{\partial}{\partial \hat{x}}\hat{u} + g\cos\theta\frac{\partial}{\partial \hat{x}}\hat{h} = g\sin\theta, \quad (2)$$

where $\hat{x}$ is the downstream coordinate, $\hat{t}$ is time, g is the magnitude of gravitational acceleration, $\hat{u}(\hat{x}, \hat{t})$ is the depth-averaged flow velocity, and $\hat{h}(\hat{x}, \hat{t})$ is the flow depth measured perpendicular to the bed. Note that we use the shallow-water equations in a non-conservative form, which is permitted since the solution to the initial-boundary-value problem investigated here is smooth. Originally, the Saint-Venant equations were derived to model flood propagation on shallow slopes and smooth topography [*Saint Venant*, 1871], but modern formulations have demonstrated that the equations can be recast to apply rigorously to steep slopes and irregular topography [*Dressler*, 1978; *Bouchut et al.*, 2003; *Keller*, 2003].

Equations (1–2) can be normalized using the following scaled variables

$$x = \frac{\hat{x}}{H_0},\ t = \sqrt{\frac{g\cos\theta}{H_0}}\hat{t},\ h = \frac{\hat{h}}{H_0},\ \text{ and } u = \frac{\hat{u}}{\sqrt{gH_0\cos\theta}},$$

where H_0 is the initial fluid depth at the dam wall. Substitution of the scaled variables into (1) and (2) yields the following dimensionless equations

$$\frac{\partial h}{\partial t} + u\frac{\partial h}{\partial x} + h\frac{\partial u}{\partial x} = 0, \tag{3}$$

$$\frac{\partial u}{\partial t} + u\frac{\partial u}{\partial x} + \frac{\partial h}{\partial x} = \tan\theta, \tag{4}$$

which can be recast in the matrix form

$$\frac{\partial}{\partial t}\mathbf{U} + \mathbf{A}\cdot\frac{\partial}{\partial x}\mathbf{U} = \mathbf{B},$$

with

$$\mathbf{U} = \begin{bmatrix} h \\ u \end{bmatrix},\ \mathbf{A} = \begin{bmatrix} u & h \\ 1 & u \end{bmatrix},\ \text{and } \mathbf{B} = \begin{bmatrix} 0 \\ \tan\theta \end{bmatrix}.$$

The matrix A has two real eigenvalues given by $\lambda_{\pm} = u \pm \sqrt{h}$, indicating that the shallow-water equations are fully hyperbolic and that $\sqrt{h}$ can be identified as the dimensionless wave celerity, $c = \sqrt{h}$. The hyperbolic system of equations can be expressed in terms of their characteristics as [*Stoker*, 1957; *Whitham*, 1974; *Chanson*, 2004]

$$\frac{d\alpha}{dt} = \tan\theta \text{ along the } \alpha\text{-characteristic curve: } \frac{dx}{dt} = u + c, \tag{5}$$

where $\alpha = u + 2c$ is the associated Riemann variable; and

$$\frac{d\beta}{dt} = \tan\theta \text{ along the } \beta\text{-characteristic curve: } \frac{dx}{dt} = u - c, \tag{6}$$

where $\beta = u - 2c$ the other Riemann variable.

2.2. Initial and boundary conditions for the dam-break problem

We consider a situation in which a dam perpendicular to the slope initially retains a reservoir behind it, as shown in Figure 1. The reservoir geometry is defined in cross section by the triangle OAB, where OA denotes the dam wall. The initial water depth is $h = h_0(x) = 1 - x/x_b$, where $x_b = -1/\tan\theta$ represents the abscissa of point B in Figure 1. At time $t = 0$, the dam collapses instantaneously and unleashes a flood of finite volume down the slope. An important difference between our formulation and that of *Fernandez-Feria* [2006] lies in the initial configuration of the flow, because *Fernandez-Feria* [2006] investigated the case of a vertical dam. Although a vertical dam is more similar to some real-world scenarios, it leads to significant mathematical difficulties when the method of characteristics is employed owing to singular behavior of the front and rear (both u and h being zero there).

Following the dam break, part of the water immediately moves downstream in the form of a forward wave, while a wave propagating upstream separates moving fluid from static fluid upslope. The downstream and upstream waves constitute moving boundaries issuing from the origin point in the $x - t$ plane (Figure 2). One boundary corresponds to the flow front, where $h = 0$ and $u = u_f$ (u_f being the front velocity, unknown for the present). The other boundary constitutes the locus of the upstream propagating wave, which travels to point B in Figure 1. Along this wave, we have $h = h(t)$ (which is also unknown at present) and $u = 0$.

Mathematically, the two moving boundaries are described by characteristic curves in the $x - t$ plane, which can be computed using (5) or (6), with $h = 0$ (forward front) and $u = 0$ (backward wave). For the forward wave, equation (5) reduces to $du/dt = \tan\theta$. The initial condition applicable with this equation is $u = 2$ at $t = 0$ because the dam collapse theoretically causes instantaneous acceleration at $t = 0$ such that the front velocity immediately becomes $u = 2$, independently of slope. Although this instantaneous acceleration appears unrealistic physically, it is a logical consequence of the shallow-water approximation, and it can be demonstrated mathematically by noting that the initial value of the Riemann variable α is 2; at early times after the dam collapse, since the flow-front depth drops to zero, this value implies that $u = 2$ at the flow front. Use of this value as the initial condition in $du/dt = \tan\theta$ yields the front velocity solution $u = t\tan\theta + 2$. Moreover, because $u = dx/dt$, we deduce that $x = \frac{1}{2}t^2\tan\theta + 2t$ is the locus of the front position in the $x - t$ plane.

To obtain the speed of the wave that propagates upstream from the dam into still water, we infer from (6) that $d(-2c)/dt = \tan\theta$ along the characteristic curve. Integration of this equation gives $c = -\frac{\tan\theta}{2}t + 1$ since at $t = 0$, we have $c = 1$. Substitution of this result into the equation defining the characteristic, $dx/dt = c$ yields $x = \frac{\tan\theta}{4}t^2 - t$ as the equation governing propagation of the backward wave in the $x - t$ plane. According to this equation, point B in Figures 1 and 2 is reached by the backward wave at time $t_b = 2\text{cotan}\theta$.

Once point B is reached, a new wave issues from point B and defines the speed of the moving tail of the volume of fluid as it descends the slope. Propagation of this wave follows the trajectory BC in Figure 2. At the tail margin, the condition $h = 0$ ($c = 0$) applies, just as at the front of the forward wave. At point B, the initial conditions for the characteristic equation are $x = x_b = -\text{cotan}\theta$, $t = t_b = 2\ \text{cotan}\theta$, $h = 0$ and $u = 0$. Substituting $c = 0$ in (5) and integrating the resulting equation $du/dt = \tan\theta$ yields the wave velocity $u = \tan\theta(t - t_b) = t\tan\theta - 2$. Integrating this equation once again yields the equation describing the position of the moving tail in the $x - t$ plane:

$$x = \tan\theta\left(\frac{1}{2}t^2 - tt_b + \frac{t_b^2}{2}\right) + x_b = \frac{t^2}{2}\tan\theta - 2t + \text{cotan}\theta.$$

Tables 1 and 2 summarize all the equations defining the boundaries of the moving fluid, and Figure 2 illustrates the position of the boundaries in the $x - t$ plane.

Some key physical implications of the boundary equations listed in Tables 1 and 2 deserve special mention. First, once motion of the head and tail begins from their respective initial conditions, each boundary propagates downslope with an acceleration identical to that of a frictionless point mass moving along the slope. This finding implies that the boundary speeds are uninfluenced by the presence of adjacent fluid after motion commences. Second, the speed of the advancing flow front always exceeds that of the advancing tail by 4 for $t > t_b$. The difference in speeds is inherited from the difference in initial conditions affecting the head and tail, and it implies that the traveling wave of fluid continuously elongates at a constant rate. This constant elongation would not occur, of course, in a flow with frictional dissipation.

3. Homogenization and hodograph transformation

In order to make the governing equations homogeneous and simplify calculations, we use a change in variables so that the effects of gravitational acceleration do not appear explicitly:

$$\tilde{\xi} = x - \frac{\tan\theta}{2}t^2,\ \tilde{t} = t,\ \tilde{v} = u - t\tan\theta, \text{ and } \tilde{h} = h, \tag{7}$$

Use of these substitutions in (3) and (4) yields

$$\frac{\partial h}{\partial t} + v\frac{\partial h}{\partial \xi} + h\frac{\partial v}{\partial \xi} = 0, \tag{8}$$

$$\frac{\partial v}{\partial t} + v\frac{\partial v}{\partial \xi} + \frac{\partial h}{\partial \xi} = 0, \tag{9}$$

where the tilde has been removed to simplify notation. The characteristic form of these equations is now

$$\frac{dr}{dt} = 0 \text{ along the } r\text{-characteristic curve: } \frac{d\xi}{dt} = v + c, \tag{10}$$

where $r = v + 2c$ is a Riemann invariant, and

$$\frac{ds}{dt} = 0 \text{ along the } s\text{-characteristic curve: } \frac{d\xi}{dt} = v - c, \tag{11}$$

where $s = u - 2c$ is the other Riemann invariant.

The next step is linearization in order to use analytical methods available for linear partial differential equations [*Garabedian*, 1964]. Transformation of the governing equations into quasi-linear equations is made possible by using hodograph variables. That is, instead of seeking solutions in the form $h(\xi, t)$ and $v(\xi, t)$, we switch the dependent and independent variables and seek solutions in the form $\xi(v, h)$ and $t(v, h)$ or, more precisely, $\xi(r, s)$ and $t(r, s)$ since we have

$$v = \frac{1}{2}(r + s) \text{ and } \sqrt{h} = \frac{1}{4}(r - s). \tag{12}$$

Denoting the Jacobian of the transformation by $J = \xi_h t_v - \xi_v t_h$, we obtain

$$h_\xi = \frac{t_v}{J},\ v_\xi = -\frac{t_h}{J}\ h_t = -\frac{\xi_v}{J},\ \text{and}\ v_t = \frac{\xi_h}{J}.$$

The transformation is reversible provided $J \neq 0$ and $1/J \neq 0$. This condition is satisfied here except at the flow boundaries, but since the solution is known there (as summarized in Table 2), this restriction presents no difficulty. With the new variables, the homogeneous governing equations (8) and (9) reduce to

$$-\frac{\partial \xi}{\partial v} + v\frac{\partial t}{\partial v} - h\frac{\partial t}{\partial h} = 0, \tag{13}$$

$$\frac{\partial \xi}{\partial h} + \frac{\partial t}{\partial v} - v\frac{\partial t}{\partial h} = 0. \tag{14}$$

Equations (13) and (14) can be solved using the method of characteristics. The equation of an r-characteristic in the plane $r - s$ is given by

$$\frac{\partial \xi}{\partial s} = \frac{3r + s}{4}\frac{\partial t}{\partial s}, \tag{15}$$

which was deduced from Eq. (10) using $d\xi = \xi_s ds$ and $dt = t_s ds$ since r is constant. Similarly, we obtain for the s-characteristic equation

$$\frac{\partial \xi}{\partial r} = \frac{3s + r}{4}\frac{\partial t}{\partial r}. \tag{16}$$

We next derive a single equation governing t. Differentiating Eq. (15) with respect to r and Eq. (16) with respect to s, then finding the difference of the two resulting equations, we obtain the equation for t:

$$L[t] = 0 \text{ where } L[t] = \frac{\partial^2 t}{\partial r \partial s} - \frac{3}{2(r - s)}\left(\frac{\partial t}{\partial r} - \frac{\partial t}{\partial s}\right). \tag{17}$$

A similar equation can be obtained for ξ, but its form is more complicated and it is more fruitful to compute t by solving Eq. (17) and then using one of the characteristic equations

(15) or (16) to find ξ. Equation (17) is a linear hyperbolic partial differential equation of second order, which arises in a number of contexts in gas dynamics and hydrodynamics and for which solutions are known in terms of Riemann functions [*Courant and Friedrich*, 1948; *Garabedian*, 1964; *Kevorkian*, 2000]. The boundary conditions for Eq. (17) are specified along curves OA, OB, and BC (see Table 1).

4. Riemann formulation

Next we exploit the linearity of Eq. (17) and use an integral representation to relate t to its auxiliary conditions. If we integrate Eq. (17) over a finite domain $\mathcal{D}$ whose oriented contour is denoted by Γ, we obtain area integrals that by themselves yield little insight. However, if we transform these area integrals into boundary integrals using Green's theorem, then part of the problem is solved. In this context, Riemann's formulation involves introducing an adjoint differential operator $N(\tau)$, which enables us to write [*Garabedian*, 1964; *Zauderer*, 1983]

$$\tau L[t] - tN[\tau] = \nabla \cdot \mathbf{U} = \frac{\partial U}{\partial r} + \frac{\partial V}{\partial s},$$

where $\mathbf{U} = (U, V)$ is a vector field. In this way, we obtain

$$\int_{\mathcal{D}} (\tau L[t] - tN[\tau]) dr ds = \int_{\Gamma} \mathbf{U} \cdot \mathbf{n} d\eta, \tag{18}$$

where $\mathbf{n}$ is an outward normal vector along Γ and $d\eta$ is a curvilinear abscissa such that $\mathbf{n}d\eta = (ds, -dr)$. For this decomposition to hold, we must define N, U, and V as follows

$$N[\tau] = \frac{\partial^2 \tau}{\partial r \partial s} + \frac{3}{2(r-s)}\left(\frac{\partial \tau}{\partial r} - \frac{\partial \tau}{\partial s}\right) - \frac{3\tau}{(r-s)^2}. \tag{19}$$

$$U = -\frac{3}{2}\frac{1}{r-s} t\tau + \frac{\tau}{2}\frac{\partial t}{\partial s} - \frac{t}{2}\frac{\partial \tau}{\partial s}, \tag{20}$$

$$V = \frac{3}{2}\frac{1}{r-s} t\tau + \frac{\tau}{2}\frac{\partial t}{\partial r} - \frac{t}{2}\frac{\partial \tau}{\partial r}. \tag{21}$$

We now consider a geometric domain $\mathcal{D}$ in the form a quadrilateral MPOQ, as depicted in Fig. 3. The value of t is known along PO (point O corresponds to point O in the $x-t$ plane) and OQ (see Table 1). Since we are free to choose the function τ, we pose

$$N[\tau] = 0, \tag{22}$$

with the boundary conditions

$$\tau(a,b) = 1,\ \frac{\partial \tau}{\partial s} = -\frac{3\tau}{2(r-s)} \text{ on } r = a, \text{ and } \frac{\partial \tau}{\partial r} = \frac{3\tau}{2(r-s)} \text{ on } s = b, \tag{23}$$

These equations remove the dependency on v in the boundary integrals along PM and QM. The solution of (22) satisfying these boundary conditions may be written as the Riemann function $R(r,\, s\,;\, a,\, b)$:

$$\tau(r,s) = R(r,\, s\,;\, a,\, b) = \frac{(r-s)^3}{(r-b)^{3/2}(s-a)^{3/2}} F\left[\frac{3}{2},\, \frac{3}{2},\, 1,\, \frac{(r-a)(s-b)}{(r-b)(s-b)}\right]. \tag{24}$$

where F is the hypergeometric function [*Abramowitz and Stegun*, 1964, p. 556]. A derivation of (24) is provided in Appendix B.

Identifying the function τ as in (24) and making use of (22), (18) becomes $\int_\Gamma \mathbf{U}\cdot\mathbf{n}d\eta = 0$. The oriented contour line Γ can be broken down into segments QM and MP, where the boundary conditions (23) hold, and the segments PO and OQ (Figure 3), leading to

$$\int_\Gamma \mathbf{U}\cdot\mathbf{n}d\eta = -\int_Q^M V dr + \int_M^P U ds - \int_P^O V dr + \int_O^Q U ds = 0. \tag{25}$$

After integrating the boundary integrals in (25) by parts and making use of (23), we rearrange the contribution along each segment of Γ as follows

$$\int_Q^M V dr \;=\; \frac{1}{2}[t\tau]_Q^M + \int_Q^M t\left(\frac{3}{2}\frac{\tau}{r-b} - \frac{\partial \tau}{\partial r}\right) dr = -\frac{1}{2}t(Q)\tau(Q) + \frac{1}{2}t(a,b), \tag{26}$$

$$\int_M^P U ds \;=\; \frac{1}{2}[t\tau]_M^P + \int_M^P t\left(-\frac{3}{2}\frac{\tau}{a-s} - \frac{\partial \tau}{\partial s}\right) ds = \frac{1}{2}t(P)\tau(P) - \frac{1}{2}t(a,b), \tag{27}$$

$$\int_P^O V dr = -\frac{1}{2}[tR]_P^O + \int_P^O R(r,\, s\,;\, a,\, b)\left(\frac{3}{2}\frac{t}{r+2} + \frac{\partial t}{\partial r}\right) dr, \tag{28}$$

$$\int_O^Q U ds = -\frac{1}{2}[tR]_O^Q + \int_O^Q R(r,\, s\,;\, a,\, b)\left(-\frac{3}{2}\frac{t}{2-s} + \frac{\partial t}{\partial s}\right) ds. \tag{29}$$

In so doing, we obtain from the right-hand sides of (26)–(29) an integral representation of t that holds for any point M $(a,\, b)$ inside the triangle OFB in the $r - s$ plane

$$t(a,\, b) = \frac{1}{2}t(P)R(P\,;\, M) + \frac{1}{2}t(Q)R(Q\,;\, M) + \int_P^Q (U ds - V dr).$$

Since on the boundaries PO and OQ we have $t_r = -\text{cotan}\theta/2$ and $t_s = 0$, respectively, we can reduce the equation for t to

$$t(a,\, b) = \text{cotan}\theta \int_2^a R(r,\, -2\,;\, a,\, b)\frac{2-5r}{4(r+2)} dr. \tag{30}$$

The variable ξ is then computed by integrating an s-characteristic, i.e., Eq. (16)

$$\xi(r|s = cst) = \frac{1}{4}(3s + r)t(r,\, s) + \frac{1}{4}\int_r^2 t(r',\, s)dr', \tag{31}$$

where we have taken into account the boundary condition $\xi = 0$ at $t = 0$.

Although equations (30) and (31) are not fully explicit expressions, these exact integral solutions can be evaluated numerically without any difficulty by using computing software such as Mathematica. The Mathematica notebook used to plot the figures in this paper is available online from our website (http://lhe.epfl.ch). The solutions can also be expressed in terms of Legendre functions and computed using tabulated values. Note that when $\theta \to 0$, time t tends toward infinity, which means that with this solution, we cannot recover the solution calculated by *Hogg* [2006] for a horizontal plane. This restriction results from the differing upstream boundary condition in the two problems. For a horizontal bottom, part of the fluid remains in the reservoir and the velocity at point B is zero, whereas for a sloping bed, once the backward wave has reached the upstream end of the reservoir, the tail of the flood wave starts moving and its velocity is nonzero (see Table 1).

Equations (30) and (31) form an implicit solution to Eqs. (8–9) that can be quite easily inverted to provide $h(\xi, t)$ and $v(\xi, t)$. Figure 4 shows the s- and r-characteristics obtained when the bed slopes at the angle $\theta = \pi/4$. Figure 5 shows the flow-depth and velocity profiles at different times after the dam collapse for $\theta = \pi/4$. The graphs of Figure 5 depict the flow depth and velocity profiles in a frame moving at velocity $t \tan\theta$. Note that the velocity variations are nearly linear and the flow depth profile is increasingly symmetric as elapsed time increases. These features are reminiscent of the parabolic-cap similarity solution of *Savage and Hutter* [1989]. A shown in Appendix C, however, the parabolic cap solution differs from the long-time asymptotic solution of the shallow-water equations we present here.

Expressing our solution in terms of the original dimensionless variables x and t is straightforward. The value of x is given by $x = \xi + \frac{1}{2}\tan\theta t^2$, while t remains unchanged. Figure 6 uses these variables to depict the flow-depth and velocity profiles at different times after the dam collapse, and figure 7 shows details of the evolution of flow depth at early times. Combining the velocity and flow depth profiles at early times makes it possible to evaluate the discharge at the dam site and thereby to obtain a hydrograph that can be used to provide initial conditions in numerical models that route floods using the shallow-water equations. Finally, note that the shape of the characteristic curves in the $x-t$ plane is significantly altered due to fluid acceleration. Figure 8 shows the β- and α-characteristics in the $x-t$ plane for $\theta = \pi/4$.

The physical variables $\hat{x}$, $\hat{t}$, $\hat{u}$, and $\hat{h}$ can be represented parametrically by using the dimensionless auxiliary variables $r = v + 2\sqrt{h}$ and $s = v - 2\sqrt{h}$ (i.e., the Riemann invariants)

$$\hat{t}(r,s) = \sqrt{\frac{H_0}{g\cos\theta}}t = \sqrt{\frac{H_0}{g\cos\theta}}\text{cotan}\theta\int_2^r R(\xi,\,-2\,;\,r,\,s)\frac{2-5\xi}{4(\xi+2)}d\xi, \tag{32}$$

$$\hat{x}(r,s) = H_0 x = \frac{1}{4}\left((3s+r)\sqrt{gH_0\cos\theta}\hat{t} + \sqrt{gH_0\cos\theta}\int_r^2 \hat{t}(\xi,\,s)d\xi + 2\sin\theta g\hat{t}^2\right), \tag{33}$$

$$\hat{u}(r,s) = \sqrt{gH_0\cos\theta}u = v\sqrt{gH_0\cos\theta} + g\hat{t}\sin\theta, \tag{34}$$

$$\hat{h}(r,s) = H_0 h, \tag{35}$$

for $r > s > -2$ and $-2 < r < 2$ and where R is the Riemann function given by Eq. (24). For $s = -2$ and $-2 < r < 2$, which apply to the backward wave for $0 < t < t_b$, we have

$$\hat{t}(r,-2) = \sqrt{\frac{H_0}{g\cos\theta}}\left(1-\frac{r}{2}\right)\text{cotan}\theta, \tag{36}$$

$$\hat{h}(r,-2) = H_0\left(1-\hat{t}\sqrt{\frac{g\cos\theta}{H_0}}\tan\theta\right). \tag{37}$$

The case $r = s$ (with $s > -2$) corresponds to $t \to \infty$, while $r = 2$ (with $s > -2$) corresponds to the initial condition before the dam breaks. The particular value $r = s = 2$ gives the position and velocity of the flow front, while $r = s = -2$ gives the position and velocity of the flow tail after the fluid has detached from point B (i.e., for $t > t_b$):

$$\hat{h}(2,2) = 0 \text{ and } \hat{u}(2,2) = g\hat{t}\sin\theta + 2\sqrt{gH_0\cos\theta}, \tag{38}$$

$$\hat{h}(-2,-2) = 0 \text{ and } \hat{u}(-2,-2) = g\hat{t}\sin\theta - 2\sqrt{gH_0\cos\theta}. \tag{39}$$

5. Conclusion

By employing the one-dimensional shallow-water equations, an accelerated reference frame, hodograph transformation, and Riemann's method, we have derived a new exact solution describing the behavior of a dam-break flood of finite volume traveling down a steep, planar slope. Although the solution assumes that the fluid is frictionless, it nonetheless provides an end-member test case suitable for assessing the accuracy and robustness of numerical methods used to simulate real floods. The solution employs an initial condition in which a triangular prism of static fluid is impounded by a dam face normal to the slope, and the flood is triggered when the dam instantaneously vanishes.

Key aspects of the motion of the flood head and tail are illustrated by some elementary features of our solution obtained directly from the untransformed shallow-water equations. For example, the solution shows that the evolving speed of the flow front is the same as that of a frictionless point mass with an initial velocity $\hat{u} = 2\sqrt{gH_0 \cos\theta}$, where g is the magnitude of gravitational acceleration, H_0 is the initial height of water behind the dam, and θ is the slope angle. Relative to motion of the flow front, motion of the tail is delayed by a time proportional to cotanθ, because motion of the tail does begin until a wave propagates upstream from the broken dam. This delay causes the downslope speed of the tail to persistently lag behind that of the front, and as a consequence of this delay and the fact that the tail subsequently accelerates like a frictionless point mass, the flood wave elongates at a constant rate. Our solution describes evolution of the elongating flood wave in terms of definite integrals that are readily evaluated using software such as Mathematica. This evaluation shows that the flood wave is initially quite asymmetric but becomes increasingly symmetric as time proceeds.

Finally, we note that extension of our solution to more complex dam-break flows involving materials other than ideal fluids may be possible. Motion of rock avalanches, snow avalanches, and debris flows, for example, obeys equations that are mathematically similar to the shallow-water equations [*Savage and Hutter*, 1989; *Pudasaini and Hutter*, 2006;

Iverson and Denlinger, 2001; *Mangeney-Castelnau et al.*, 2005; *Balmforth and Kerswell*, 2005], and these phenomena are good candidates for further analytical study. In particular, the experimental and numerical results obtained by *Greve et al.* [1994] and *Koch et al.* [1994] for dam-break avalanches of granular materials down steep chutes appear very similar to results described in this paper.

Acknowledgments. We thank Professors J.M.N.T. Gray (University of Manchester) and Randall LeVeque (University of Washington) for their helpful reviews of our work. In particular, Professor LeVeque ran his shock-capturing numerical code Tsunamiclaw (freely downloadable from http://www.amath.washington.edu/~claw/) and found excellent agreement with our solution. The work presented here was supported by the Swiss National Science Foundation under grant number 200021-105193, the competence center in Mobile Information and Communication Systems (a center supported by the Swiss National Science Foundation under grant number 5005-67322), the Competence Center in Environmental Sciences (TRAMM and APUNCH projects), and specific funds provided by EPFL (*vice-présidence à la recherche*). Use of trade names in this publication is for information purposes only and does not constitute endorsement by the U.S. Geological Survey.

Appendix A

In this paper, basal friction has been neglected. This assumption is likely to be valid in the bulk of the flow since the bottom friction contribution is usually of low magnitude compared to the inertia and pressure gradient terms in the momentum balance equation. Close to the front, this assumption no longer holds because the flow depth drops to zero. To estimate the typical extent η of the friction-affected region, the usual approach is to use a balance between friction and pressure gradient, i.e., if we use a Chézy law for representing the bottom drag, we have $\rho g\hat{h}\cos\theta\partial\hat{h}/\partial\hat{x} \sim C_d\rho\hat{u}^2$, where C_d denotes a Chézy-like coefficient, in the drag-affected region [*Whitham*, 1954; *Hogg and Pritchard*, 2004]. A difficulty arises here since $\hat{h}$ and $\hat{u}$ are not explicitly known.

To proceed further in this analysis, we first need to approximate $\hat{h}$ and $\hat{u}$ for the head. This can be readily done by making a first-order approximation of the integral representations (30) and (31) of $t(r,s)$ and $\xi(r,s)$ for the head. Then solving the resulting linear system to find r and s, we find

$$s = -\frac{2}{3} + \frac{4}{3}\frac{\xi}{t}, \tag{A1}$$

$$r = 2. \tag{A2}$$

Making use of Eq. (12) to find h and $\bar{u}$ and returning to dimensional variables, we finally obtain

$$\hat{h} = \frac{1}{9g\cos\theta}\left(\frac{\hat{x}_f - \hat{x}}{\hat{t}}\right)^2, \tag{A3}$$

$$\hat{u} = \frac{1}{3}\left(2\frac{\hat{x}}{\hat{t}} + \hat{u}_f\right), \tag{A4}$$

where $\hat{x}_f = 2\sqrt{gH_0\cos\theta}t + \frac{1}{2}gt^2\sin\theta$ denotes the front position and $\hat{u}_f = 2\sqrt{gH_0\cos\theta} + gt\sin\theta$ its velocity. A remarkable feature is that the flow-depth and velocity profiles in the close vicinity of the front have exactly the same shape as those found for the *Ritter* [1892] solution. Denoting $\eta = \hat{x}_f - \hat{x}$, we find that within the tip region ($\eta \to 0$), the dominant balance is

$$g\cos\theta \frac{\hat{h}^2}{\hat{t}^2}\frac{1}{\eta} \sim C_d \hat{u}_f^2, \tag{A5}$$

which yields

$$\eta^3 g \frac{\hat{h}^2}{\hat{t}^2} \sim 81 C_d g \cos^2\theta \hat{u}_f^2 t^3. \tag{A6}$$

At short times, $\hat{u}_f \approx 2\sqrt{gH_0\cos\theta}$ and therefore the extent of the drag-affected region scales as $t^{4/3}$

$$\eta \sim 4 C_d^{1/3} g^{2/3} \cos\theta H_0^{1/3} t^{4/3}, \tag{A7}$$

which is consistent with the scaling found for dam-break waves on horizontal planes [*Whitham*, 1954; *Hogg and Pritchard*, 2004]. At long times, $\hat{u}_f \approx gt\sin\theta$, which results in a more pronounced dependence of η on t

$$\eta \sim 4 C_d g t^2 \cos^{2/3} 2\theta. \tag{A8}$$

Appendix B

The Riemann function R can be computed as follows [*Garabedian*, 1964, see problem 9, § 5.1, p. 150]. Let us consider a partial differential equation of the form

$$v_{xy} + \frac{\lambda}{2}\frac{1}{x+y}(v_x + v_y) = 0, \tag{B1}$$

whose adjoint operator is

$$N[v] = 0, \text{ with } N[v] = v_{xy} - (av)_x - (bv)_y + cv, \text{ and } a = b = \frac{\lambda}{2}\frac{1}{x+y},$$

and where $c = 0$. Following *Garabedian* [1964], we pose

$$v = \frac{(x+y)^\lambda}{(x+\eta)^{\lambda/2}(x+\eta)^{\lambda/2}} W(\zeta), \text{ with } \zeta = \frac{(x-\xi)(y-\eta)}{(x+\eta)(y+\xi)}.$$

We find that W satisfies the equation

$$-\lambda^2 W(\zeta) + 4(1-(\lambda+1)\zeta)W'(\zeta) + \zeta(1-\zeta)W''(\zeta) = 0,$$

whose solution is

$$W(\zeta) = F\left[\frac{\lambda}{2}, \frac{\lambda}{2}, 1, \zeta\right],$$

where F is the hypergeometric function. With $\lambda = 3$, $x = r$ and $y = -s$, we find the solution to the adjoint problem (22) with N given by Eq. (19). Alternative representations (in particular, in terms of Legendre functions) can be obtained using properties of F [*Abramowitz and Stegun*, 1964, see pp. 559–562].

Appendix C

In this appendix we relate our results to those of Savage and *Savage and Hutter* [1989], who obtained similarity solutions to the shallow-flow equations for motion of finite volumes of frictional material down a uniform slope. Of particular relevance here is their parabolic cap solution, which can be obtained by seeking symmetric flow-depth and velocity profiles for the governing equations (8) and (9). In Fig. 5, we note that at sufficiently late times, the flow-depth profile is bell-shaped, while the velocity profile is nearly linear with ξ. This prompts us to seek a solution, where the velocity profile is perfectly linear and takes the value $v = \dot{\xi}_f$ at the front ($\xi = \xi_f$), i.e.,

$$v(\xi, t) = \frac{\xi}{\xi_f}\dot{\xi}_f, \tag{C1}$$

where ξ_f denotes the front position and $\dot{\xi}_f$ its velocity in the $\xi - t$ plane. For the moment, $\xi_f(t)$ is unknown; we expect that the similarity solution is the long-time asymptotic solution of the boundary initial value problem solved above and therefore assume that $\xi_f \propto 2t$. Substituting v into the momentum balance equation (9), we derive an equation for h

$$\frac{\partial h}{\partial \xi} = -\frac{\ddot{\xi}_f}{\xi_f}\xi, \tag{C2}$$

whose integration provides

$$h(\xi, t) = \frac{1}{2}\frac{\ddot{\xi}_f}{\xi_f}(\xi_f^2 - \xi^2). \tag{C3}$$

The flow-depth profile is parabolic and symmetric around $\xi = 0$. Substituting the v and h relations into the mass equation (8), we derive an equation for the front position ξ_f

$$\frac{d}{dt}(\xi_f \ddot{\xi}_f) + \dot{\xi}_f \ddot{\xi}_f = 0. \tag{C4}$$

Integrating this equation leads to the second-order differential equation

$$\xi_f^2 \ddot{\xi}_f = c_1, \tag{C5}$$

with c_1 a constant of integration, which can be determined using volume conservation

$$\mathcal{V} = \int_{-\xi_f}^{\xi_f} h(\xi, t) d\xi = \frac{2}{3}\xi_f^2 \ddot{\xi}_f = \frac{2}{3}c_1, \tag{C6}$$

where $\mathcal{V} = \frac{1}{2}|x_b| = \frac{1}{2}\text{cotan}\theta$ is the initial volume of material. We can now find ξ_f from (C5) using the boundary conditions

$$\lim_{t\to\infty} \xi_f = 2t \text{ and } \xi_f(0) = 0. \tag{C7}$$

The former boundary condition enforces behavior similarity between this solution and the one found above using the method of characteristics. The latter condition is somewhat formal, but is consistent with our objective of finding the long-time asymptotic solution. Integrating (C5) twice and using the boundary conditions (C7), we find an implicit relation relating ξ_f to t

$$4\sqrt{4\xi_f^2 - 3\xi_f\mathcal{V}} + 3\mathcal{V}\ln\left|\frac{8\xi_f - 3\mathcal{V} + 4\sqrt{4\xi_f^2 - 3\xi_f\mathcal{V}}}{3\mathcal{V}}\right| = 16t, \tag{C8}$$

which is valid for $\xi > 3\mathcal{V}/4$. Differentiating this equation with respect to t, we find that the front velocity is given by

$$\dot{\xi}_f = \frac{\sqrt{\xi_f(4\xi_f - 3\mathcal{V})}}{\xi_f}. \tag{C9}$$

We check that $\dot{\xi}_f \rightarrow 2$ when $\xi_f \infty$. The parabolic cap solution is given by

$$v(\xi, t) = \frac{\xi}{\xi_f}\dot{\xi}_f, \tag{C10}$$

$$h(\xi, t) = \frac{3}{4}\frac{\mathcal{V}}{\xi_f^3}\left(\xi_f^2 - \xi^2\right), \tag{C11}$$

with ξ_f given by (C8) and $\dot{\xi}_f$ given by (C9).

In Fig. 9, we have plotted the parabolic cap solution for $t = 100$. We also have also shown the exact solution to the shallow-water equations. A key point is that although both velocity profiles superimpose remarkably, there is a substantial difference in the shape of the surge. For the exact solution, the flow-depth profile is always acute close to the fronts since the flow-depth gradient drops to zero (see Appendix A), whereas for the similarity solution, the height gradient at the front is nonzero ($\partial h/\partial\xi = 3\mathcal{V}/(2\xi_f)$), which results in a finite front angle that the remaining flow must accommodate.

References

Abramowitz, M., and I. A. Stegun (1964), *Handbook of Mathematical Functions*, National Bureau of Standards, Washington.

Ancey, C., S. Cochard, S. Wiederseiner, and M. Rentschler (2006), Front dynamics of supercritical non-Boussinesq gravity currents, *Water Resour. Res.*, *42*, W08,424.

Ancey, C., S. Cochard, S. Wiederseiner, and M. Rentschler (2007), Existence and features of similarity solutions for supercritical non-Boussinesq gravity currents, *Physica D*, *226*, 32–54.

Balmforth, N. J., and R. R. Kerswell (2005), Granular collapse in two dimensions, *J. Fluid Mech.*, *538*, 399–428.

Bouchut, F., A. Mangeney-Castelnau, B. Perthame, and J. P. Vilotte (2003), A new model of Saint Venant and Savage-Hutter type for gravity driven shallow flows, *C. R. Acad. Sci. Paris sér. I*, *336*, 531–536.

Carrier, G. F., and H. P. Greenspan (1958), Water waves of finite amplitude on a sloping beach, *J. Fluid Mech.*, *4*, 97–109.

Chanson, H. (2004), *The Hydraulics of Open Channel Flow: An Introduction*, 2nd ed., Elsevier Butterworth Heinemann, Amsterdam.

Chanson, H. (2006), Analytical solutions of laminar and turbulent dam break wave, in *International Conference on Fluvial Hydraulics River Flow 2006*, vol. 1, edited by R. M. L. Ferreira, E. C. T. L. Alves, J. G. A. B. Leal, and A. H. Cardoso, pp. 465–474, Lisbon, Portugal.

Costa, J. E. (1988), Floods from dam failure, in *Flood Geomorphology*, edited by V. R. Baker, R. C. Kochel, and P. C. Patton, pp. 439–461, Wiley, New York.

Courant, R., and K. O. Friedrich (1948), *Supersonic Flow and Shock Waves*, Intersciences Publishers, New York.

Daly, E., and A. Porporato (2004a), Similarity solutions of nonlinear diffusion problems related to the mathematical hydraulics and the Fokker-Planck equation, *Phys. Rev. E*, *70*, 056,303.

Daly, E., and A. Porporato (2004b), A note on groundwater flow along a hillslope, *Water Resour. Res.*, *40*, W01,601.

Dressler, L. (1952), Hydraulic resistance effect upon the dam-break functions, *J. Res. Natl Bur. Stand.*, *49*(3), 217–225.

Dressler, R. F. (1978), New nonlinear shallow-flow equations with curvature, *J. Hydraul. Res.*, *16*, 205–222.

Dressler, R. H. (1958), Unsteady non-linear waves in sloping channels, *Proc. R. Soc. London ser. A*, *247*, 186–198.

Fernandez-Feria, R. (2006), Dam-break flow for arbitrary slopes of the bottom, *J. Eng. Math.*, *54*, 319–331.

Garabedian, P. R. (1964), *Partial Differential Equations*, John Wiley & Sons, New York.

Greve, R., T. Koch, and K. Hutter (1994), Unconfined flow of granular avalanches along a partly curved surface. I. Theory, *Proc. R. Soc. London ser. A*, *445*, 399–413.

Hogg, A. J. (2006), Lock-release gravity currents and dam-break flows, *J. Fluid Mech.*, *569*, 61–87.

Hogg, A. J., and D. Pritchard (2004), The effects of hydraulic resistance on dam-break and other shallow inertial flows, *J. Fluid Mech.*, *501*, 179–212.

Hunt, B. (1983), Perturbation solution for dam-break floods, *J. Hydraul. Eng.*, *110*, 1053–1071.

Iverson, R. M., and R. P. Denlinger (2001), Flow of variably fluidized granular masses across three-dimensional terrain. 1. Coulomb mixture theory, *J. Geophys. Res.*, *106*, 537–552.

Karelsky, K. V., V. V. Papkov, A. S. Petrosyan, and D. V. Tsygankov (2000), The initial discontinuity decay problem for shallow water equations on slopes, *Phys. Lett. A*, *271*, 349–357.

Keller, J. B. (2003), Shallow-water theory for arbitrary slopes of the bottom, *J. Fluid Mech.*, *489*, 345–348.

Kerswell, R. R. (2005), Dam break with Coulomb friction: a model for granular slumping?, *Phys. Fluids*, *17*, 057,101.

Kevorkian, J. (2000), *Partial Differential Equations, Analytical Solution Techniques*, Springer, New York.

Koch, T., R. Greve, and K. Hutter (1994), Unconfined flow of granular avalanches along a partly curved surface. II. Experiments and numerical computations, *Proc. R. Soc. London ser. A*, *445*, 415–435.

Mangeney, A., P. Heinrich, and R. Roche (2000), Analytical solution for testing debris avalanche numerical models, *Pure Appl. Geophys.*, *157*, 1081–1096.

Mangeney-Castelnau, A., B. Bouchut, J. P. Vilotte, E. Lajeunesse, A. Aubertin, and M. Pirulli (2005), On the use of Saint-Venant equations for simulating the spreading of a granular mass, *J. Geophys. Res.*, *110*, B09,103.

Peregrine, D. H., and S. M. Williams (2001), Swash overtopping a truncated plane beach, *J. Fluid Mech.*, *440*, 391–399.

Pudasaini, S. P., and K. Hutter (2006), *Avalanche Dynamics*, Springer, Berlin.

Ritter, A. (1892), Die Fortpflanzung der Wasserwellen, *Zeit. Vereines Deutsch. Ing.*, *36*(33), 947–954.

Saint Venant, B. (1871), Théorie du mouvement non permanent des eaux, avec application aux crues des rivières et à l'introduction des marées dans leur lit, *C. R. Acad. Sci. Paris sér. I*, *173*, 147–154– 237–240.

Savage, S. B., and K. Hutter (1989), The motion of a finite mass of granular material down a rough incline, *J. Fluid Mech.*, *199*, 177–215.

Shen, M. C., and R. E. Meyer (1963), Climb of a bore on a beach. Part 3. Run-up, *J. Fluid Mech.*, *16*, 113–125.

Stoker, J. J. (1957), *Water Waves*, Interscience Publishers, New York.

Whitham, G. B. (1954), The effects of hydraulic resistance in the dam-break problem, *Proc. R. Soc. London ser. A*, *227*, 399–407.

Whitham, G. B. (1974), *Linear and Nonlinear Waves*, John Wiley & Sons, New York.

Zauderer, E. (1983), *Partial Differential Equations of Applied Mathematics*, Pure and Applied Mathematics, John Wiley & Sons, New York.

Zoppou, C., and S. Roberts (2003), Explicit schemes for dam-break simulations, *J. Hydraul. Eng.*, *129*, 11–34.

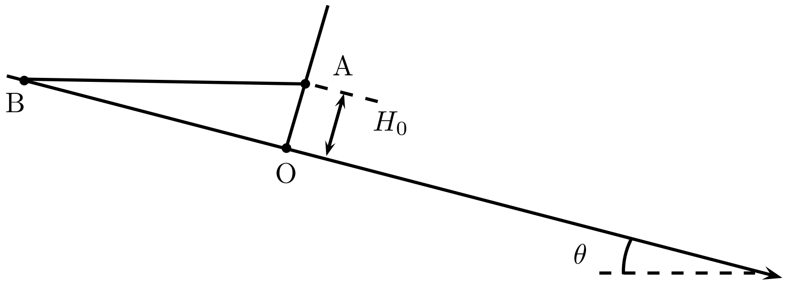

Figure 1. The initial configuration of the reservoir before the dam collapse.

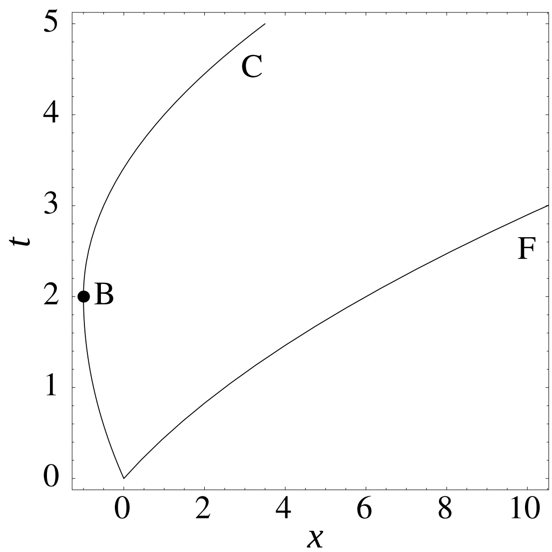

Figure 2. Characteristics corresponding to the boundaries of the moving fluid volume. Computation is for slope angle $\theta = \pi/4$.

Table 1. Features of the boundaries delimiting the fluid domain.

	c	u	v	ξ	r	s
OF	0	$t\tan\theta+2$	2	$2t$	2	2
OB	$1-t\tan\theta/2$	0	$-t\tan\theta$	$-t^2\tan\theta/4-t$	$2(1-t\tan\theta)$	-2
BC	0	$t\tan\theta-2$	-2	$-2t+\text{cotan}\theta$	-2	-2

Table 2. Equations of the boundaries delimiting the fluid domain.

	x	t range
OF	$\frac{t^2}{2}\tan\theta+2t$	$t\geq 0$
OB	$\frac{t^2}{4}\tan\theta-t$	$0\leq t\leq 2\text{cotan}\theta$
BC	$\frac{t^2}{2}\tan\theta-2t+\text{cotan}\theta$	$t\geq 2\text{cotan}\theta$

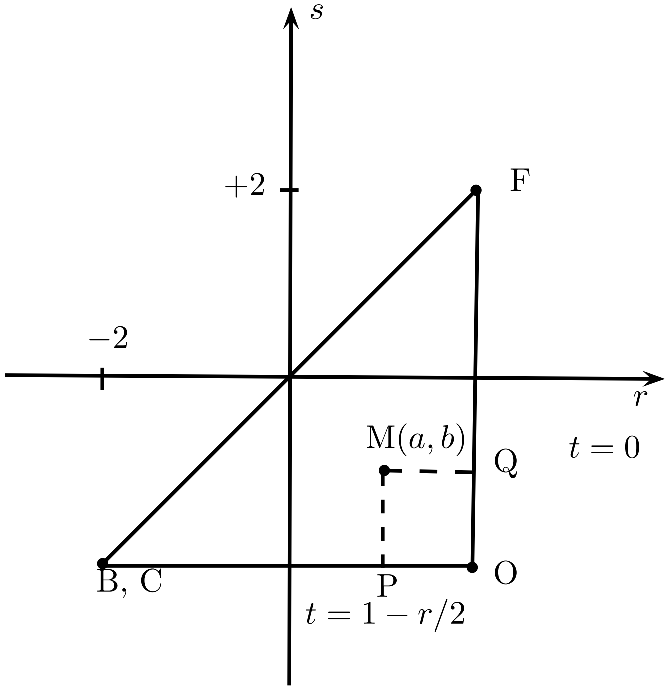

Figure 3. Computation domain in the $r - s$ plane.

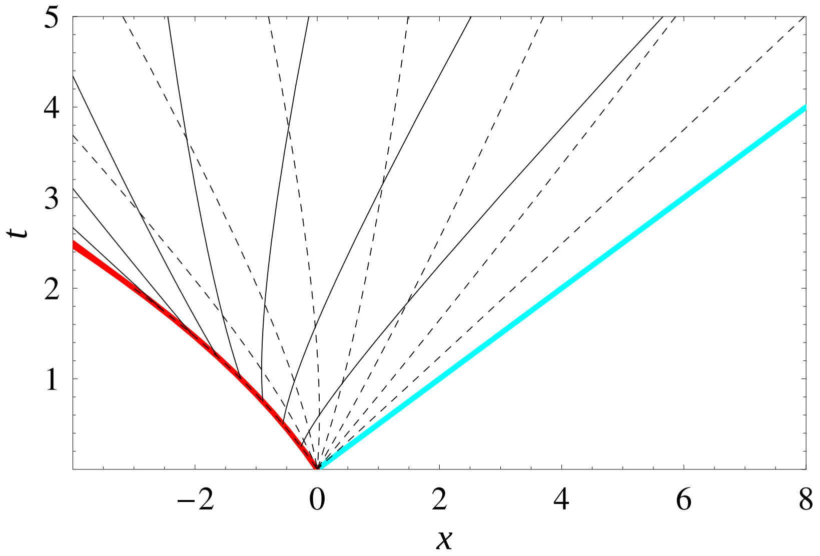

Figure 4. Characteristics in the $\xi - t$ plane for slope angle $\theta = \pi/4$. The r-characteristics are shown as solid lines for r values ranging from 2 to -2, with an increment of 0.5. The s-characteristics are shown as dashed lines for s values ranging from 2 to -2, with an increment of 0.5.

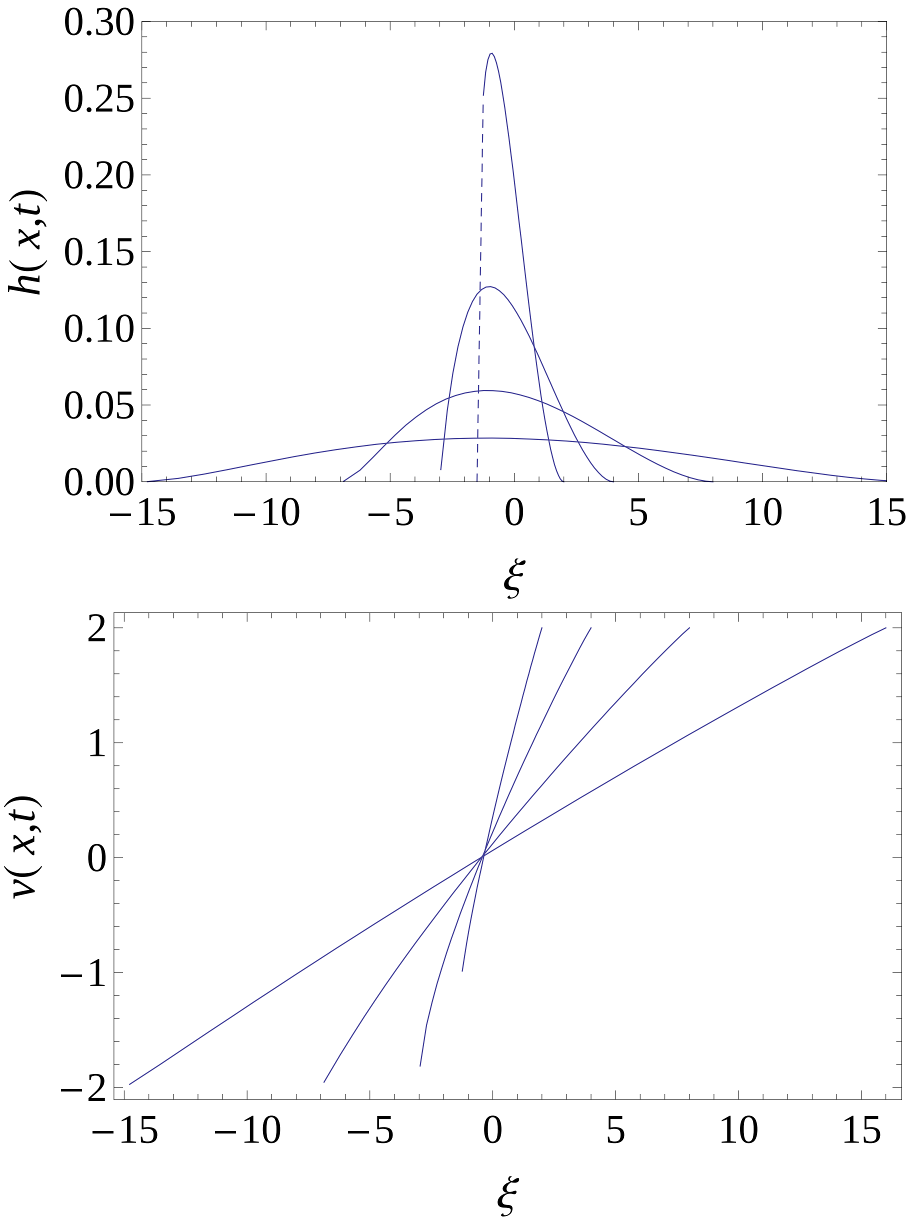

Figure 5. Flow depth and velocity profiles in the $\xi - t$ plane for slope angle $\theta = \pi/4$. Profiles are shown for times $t = 1,\ 2,\ 4,\ 8$. The dashed line represents the initial flow depth (still water).

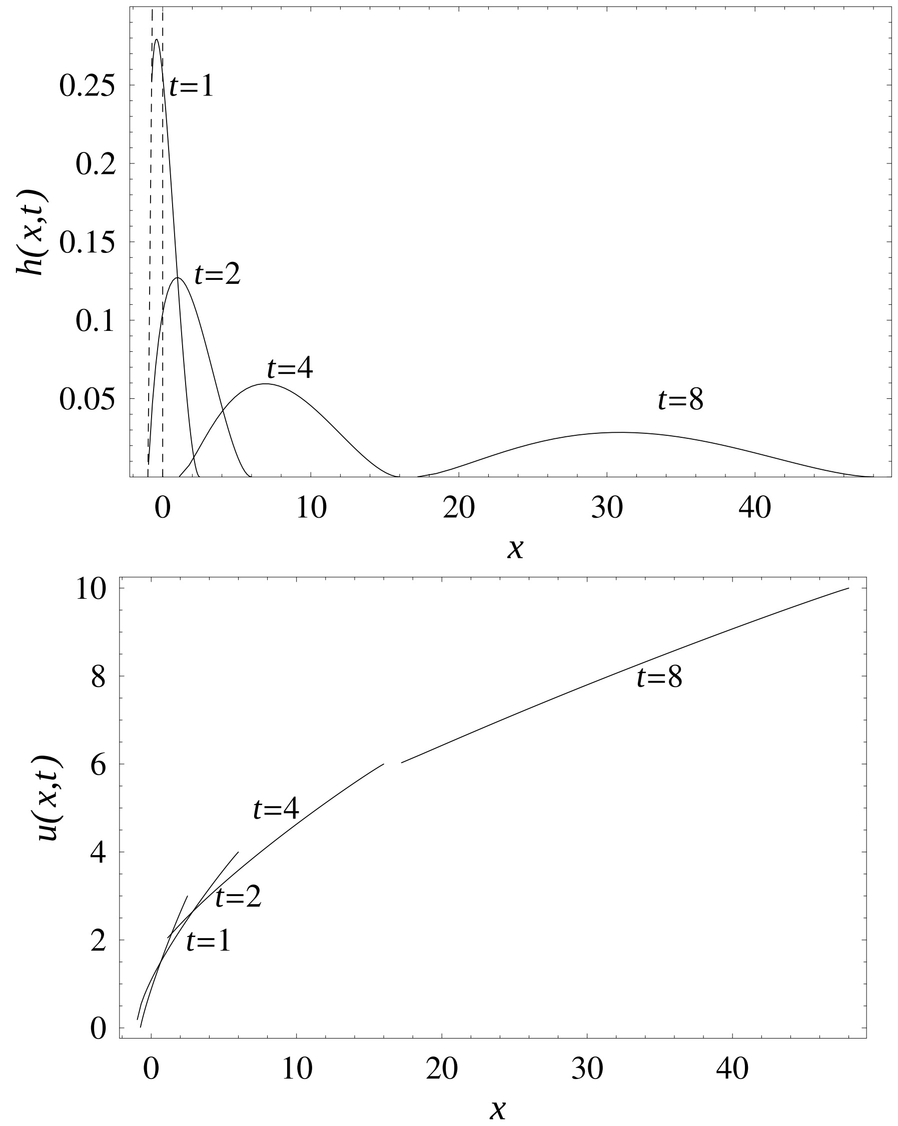

Figure 6. Flow depth and velocity profiles in the $x-t$ plane for slope angle $\theta = \pi/4$. Profiles are shown for times t = 1, 2, 4, 8. The dashed line represents the initial flow depth.

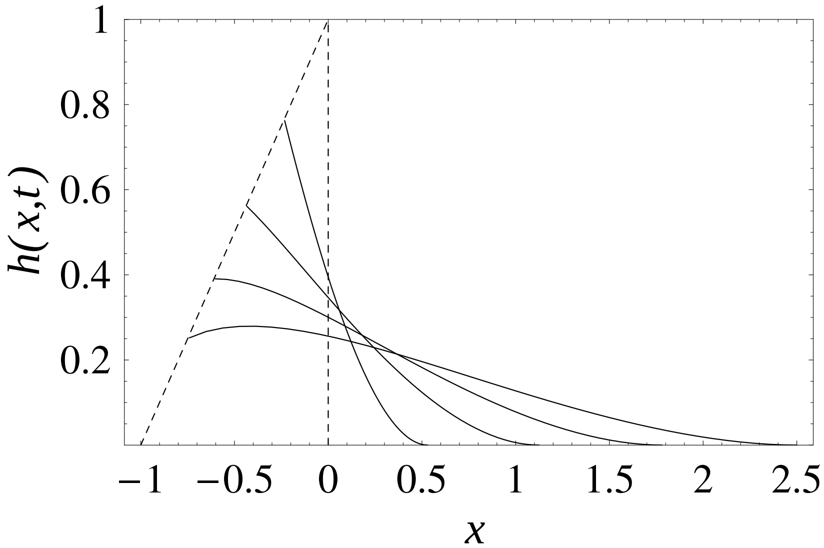

Figure 7. Flow depth profiles in the $x - t$ plane for slope angle $\theta = \pi/4$. Profiles are shown for times $t = 0.25$, 0.5, 0.75,1. The dashed line represents the initial flow depth.

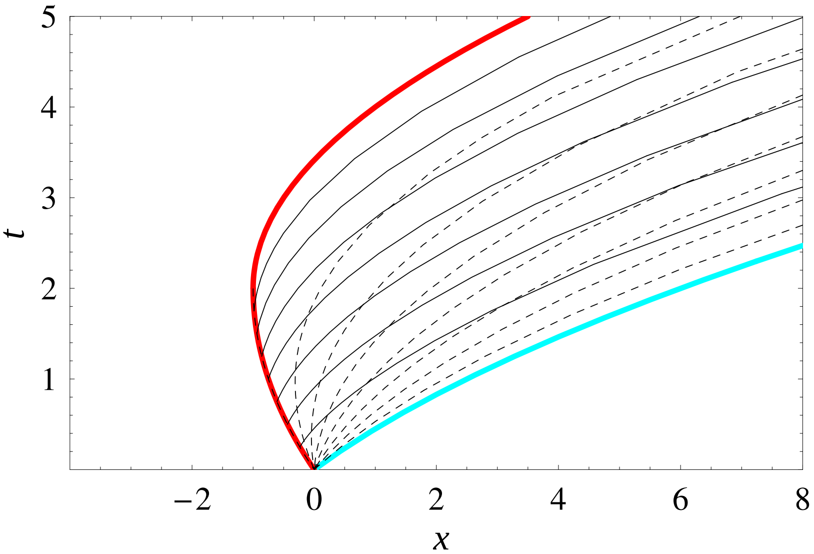

Figure 8. Characteristics in the $x - t$ plane for slope angle $\theta = \pi/4$. The α-characteristics are shown as solid lines for α values ranging from 2 to -2, with an increment of 0.5. The β-characteristics are shown as dashed lines for β values ranging from 2 to -2, with an increment of 0.5.

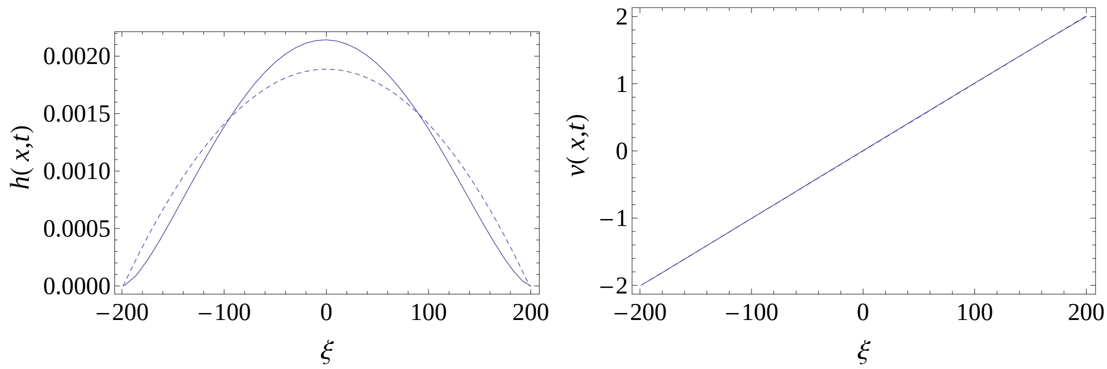

Figure 9. comparison between the exact solution to the shallow-water equations (solid line) given implicitly by equations (30) and (31) and the parabolic cap solution (dashed curve) given by equations (C10) and (C11) at $t = 100$. On the left: flow-depth profile; on the right: flow-depth averaged velocity.